Supporting Information

Tree-inspired ultra-rapid steam generation and simultaneous energy harvesting at weak illumination

Wenjing Tu,† Zhenzhen Wang,† Qingyao Wu, Hui Huang, Yang Liu, Mingwang Shao*, Bowen Yao*, Zhenhui Kang**

1. Supplementary Methods

Materials

Polyvinyl alcohol 124 (PVA 124) and liquid paraffin were purchased from Sinopharm Chemical Reagent Co., Ltd. Sorbitan monooleate (span 80) was supplied by Shanghai Macklin Biochemical Co., Ltd. Hydrochloric acid (HCl) and hydrazine hydrate solution (80%) were obtained from Chinasun Specialty Products Co., Ltd. Glutaraldehyde (50%) and carboxymethyl cellulose (CMC) was bought from Aladdin (Shanghai, China). Sodium chloride (NaCl), magnesium chloride hexahydrate ($MgCl_2 \cdot 6H_2O$), magnesium sulfate anhydrous ($MgSO_4$), calcium sulfate dihydrate ($CaSO_4 \cdot 2H_2O$), potassium sulfate (K_2SO_4) and potassium bromide (KBr) were purchased from Sinopharm Chemical Reagent Co., Ltd. All of the chemicals were utilized directly without further purification.

Synthesis of control PVA and PVA-rCDs monolithic hydrogel

4 mL PVA (5 wt%) aqueous solution, 0.5 mL HCl and 0.25 mL glutaraldehyde (50 wt%) was mixed together, followed by shaking vigorously to form homogenous solution. The mixture was transferred to a container, and the gelation was carried out for 3 h. The obtained gel was purified by immersing in deionized water overnight. PVA-rCDs monolithic hydrogel was synthesized following the same procedure above, except that 31.6 mg of rCDs was added into 4 mL 5 wt% PVA solution.

Preparation of artificial seawater

Artificial seawater with salinity of 3.5 % was prepared by dissolving 27.2 g NaCl, 3.8 g $MgCl_2 \cdot 6H_2O$, 1.7 g $MgSO_4$, 1.4 g $CaSO_4 \cdot 2H_2O$, 0.6 g K_2SO_4, and 0.1 g KBr in 1 L deionized water.[1]

Thermal conductivity measurement

The thermal conductivities of both PCM and PCB samples in dry and wet conditions were measured via an infrared (IR) imaging method.[2,3] A sandwich structure, sample as the embedded part between two pieces of quartz glasses, was placed on a heating panel (as a heat source), through which the temperature gradient across the sample-cored sandwich structures could be controlled. And the air on the other side served as a cold source. The thermal

equilibrium of the system was achieved when the fluctuation of temperature is negligible. The IR camera was utilized to monitor temperatures at three interfaces: heating plate-glass bottom (T_1), bottom glass-sample (T_2), sample-top glass (T_3). The temperature gradient (dT/dx) can be observed in the vertical direction of the structure. And the heat flux (q) across the sandwich structure was calculated by the Fourier equation:

$$q = -k_1 \frac{dT}{dx} = -k_1 \frac{T_2 - T_1}{d_1}$$

k_1 is the thermal conductivity of quartz glass (1.05 W m^{-1} K^{-1}), d_1 is the thickness of the glass (In this work, d_1=2 mm). After obtaining the heat flux value, thermal conductivity of our test sample (k) were calculated by the following formula:

$$k = -q \frac{d_2}{T_3 - T_2}$$

k and d_2 is the thermal conductivity and thickness of the sample. And all the thickness was measured by a thickness gauge. The thermal conductivity was gained by fitting the testing values.

Water transport experiment

Construction of the root and xylem system

Tree roots absorb water from the soil by osmosis. Since the water potential in surrounding soil is higher than that in the cytoplasm of root hair cells, water tend to move down the potential gradient. In addition, osmosis occurs because of the presence of the semi-permeable membrane of the root hair cell's surfaces.[4-6] Imitating the water uptake behavior of roots, forward osmosis (FO) process was employed to construct the root system of the artificial tree. Moreover, tree xylems transport water and soluble mineral nutrients via tracheids and vessel elements, which form interconnected channels after being mature.[7,8] A latex tube was chosen to vertically install on the artificial root device to act as the xylem for continuous water conduction.

FO experiment

A flat-sheet commercially available polyamide coating thin film composite (TFC) membrane (Guochu technology (Xiamen) Co., Ltd) with an effective separation area of 15 cm^{-2}, was used in the experiment to separate two solutions. Deionized water and 3.5 wt% NaCl solution (~0.6 M) as the feed solutions were used to simulate lake water and sea water, respectively. The more concentrated NaCl draw solutions were prepared to exact water from the feed solutions. And the corresponding water flux was recorded.

2. Supplementary Figures

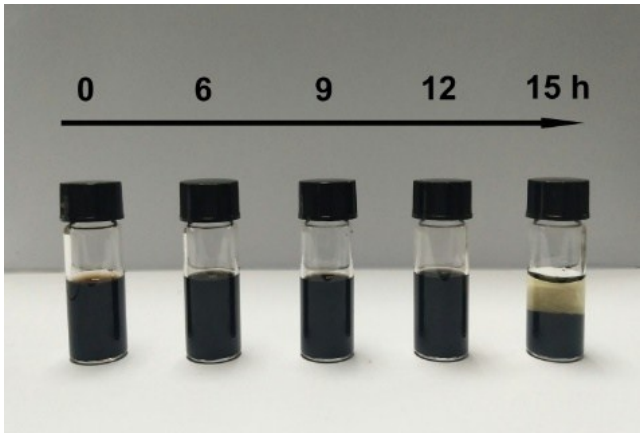

Figure S1. Photographs of CDs reduced via hydrazine hydrate for different time.

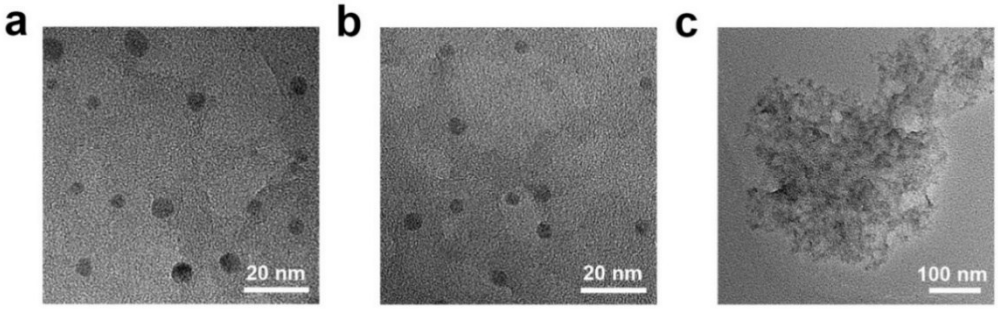

Figure S2. TEM image of (a) rCDs-6 h, (b) rCDs-9 h and (c) rCDs-15 h.

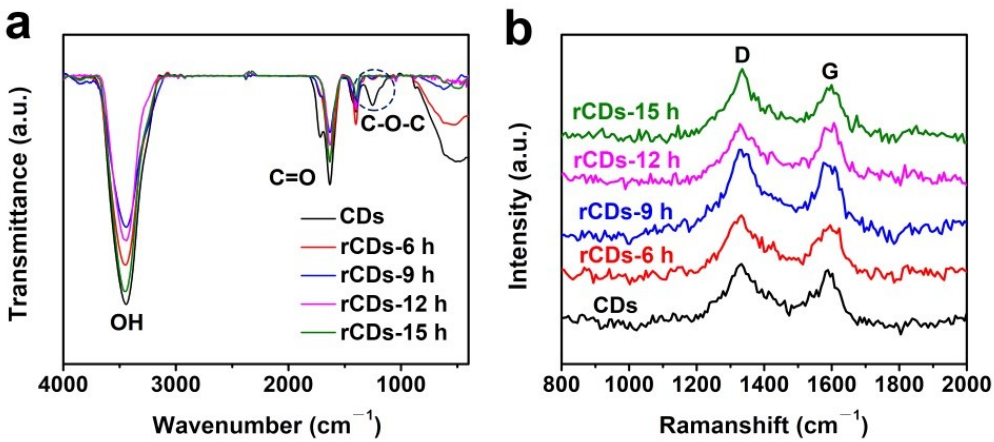

Figure S3. (a) FTIR and (b) Raman spectra of CDs, rCDs-6, rCDs-9, rCDs-12, rCDs-15 h.

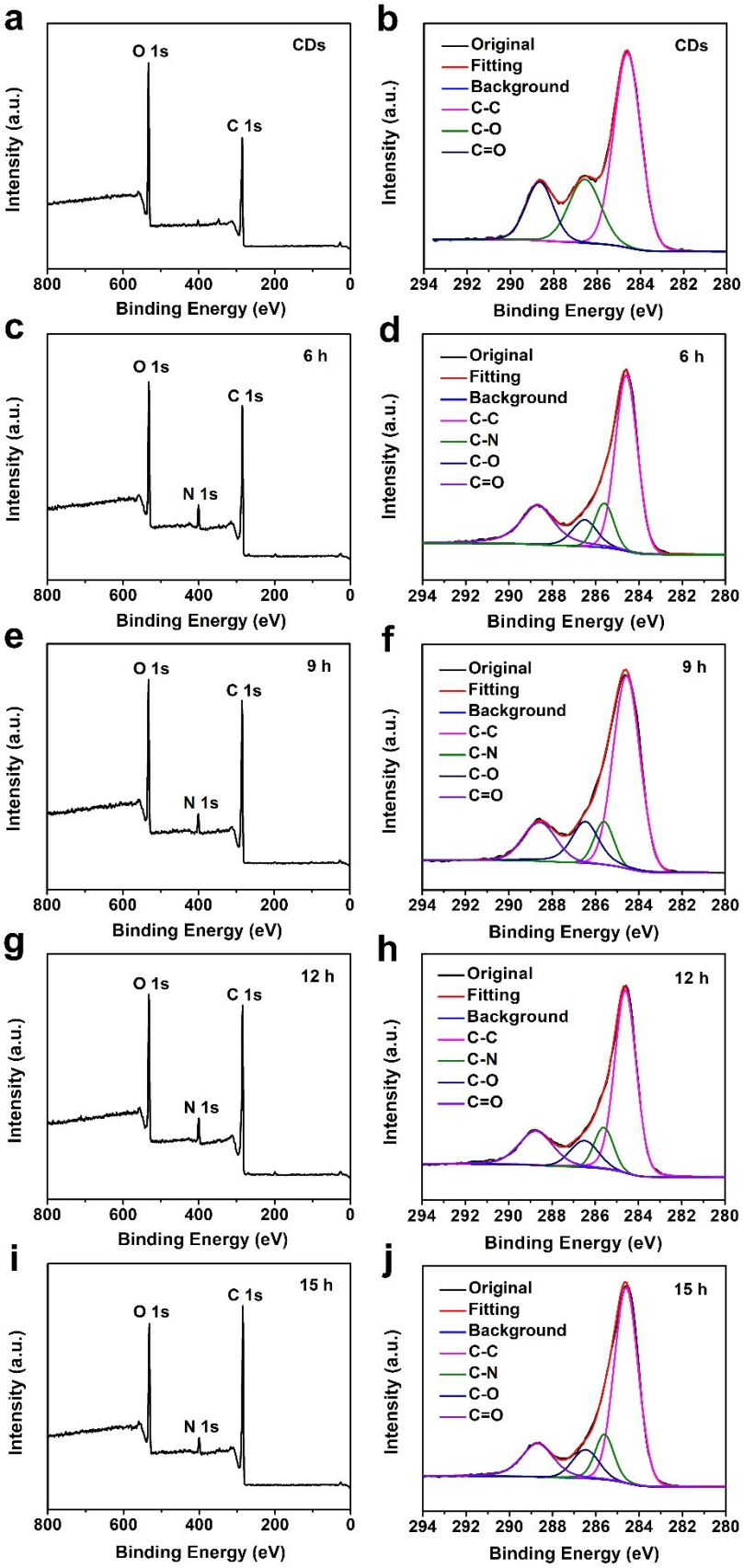

Figure S4. XPS full survey spectra, high-resolution C 1s XPS spectra of (a)-(b) CDs, (c)-(d) rCDs-6 h, (e)-(f) rCDs-9 h, (g)-(h) rCDs-12 h and (i)-(j) rCDs-15 h.

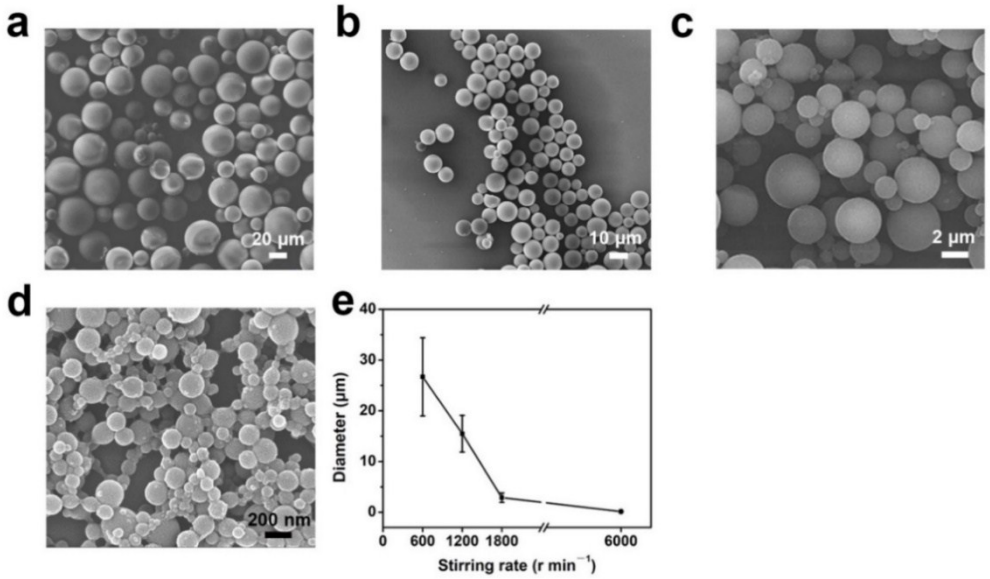

Figure S5. SEM images of PVA microgels prepared under stirring rate of (a) 600 r, (b) 1200 r, (c) 1800 r, (d) 6000 r. (e) Plot of PVA microgel diameters versus stirring rates.

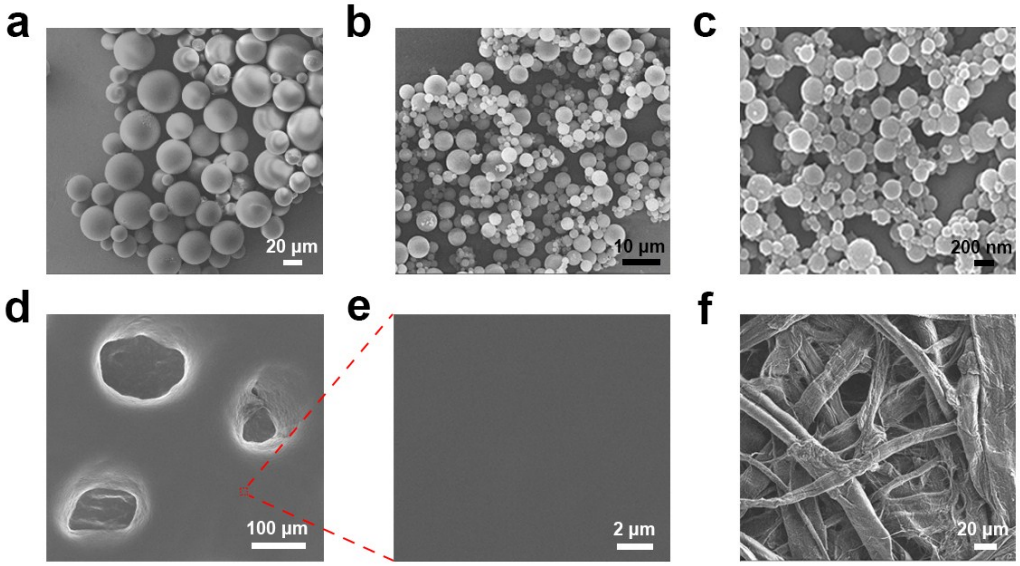

Figure S6. SEM images of PVA-rCDs microgels prepared under stirring rate of (a) 600 r, (b) 1800 r, (c) 6000r. (d)-(e) SEM images of PVA-rCDs monolithic hydrogel at different magnifications. (f) SEM image of the cellulous paper.

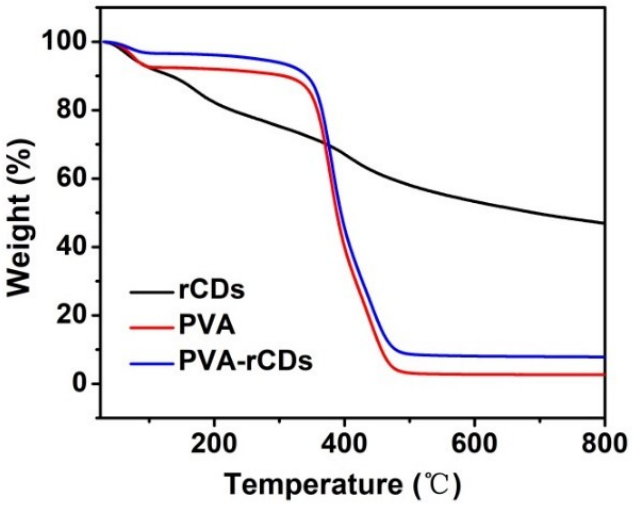

Figure S7. The TGA of rCD, pure PVA microgels and PVA-rCDs microgels. The thermogravimetric analysis (TGA) of PVA, rCDs and PVA-rCDs were conducted to analyze their chemical components. Before performing the TGA measurement, all the samples were dried at 60 ℃. We note that the the three samples show initial weight loss over the temperature range of 30~120 ℃, which was ascribe to the removeral of the physisorption water. In the subsequent region, the weight of PVA was quickly lost from 240 ℃ to 330 ℃, related to the decomposition of the polymer chains. While rCDs delivers gradually weight loss from 240 ℃ to 800 ℃ coresponding to their slow degradation. In the case of adding rCDs in PVA matrix, the decomposition behavior of the composites slightly differs by presenting the residual weight, which is associated with the remaining rCDs.

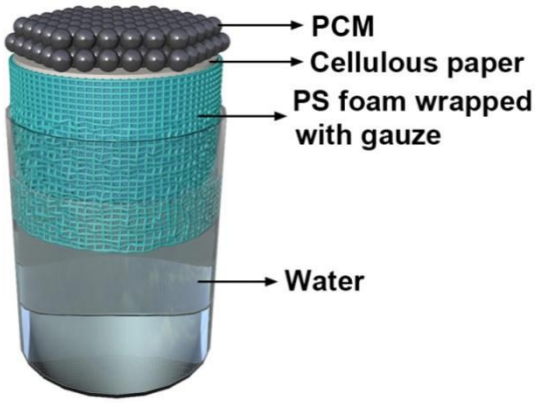

Figure S8. Structural model of the PCM-based evaporator.

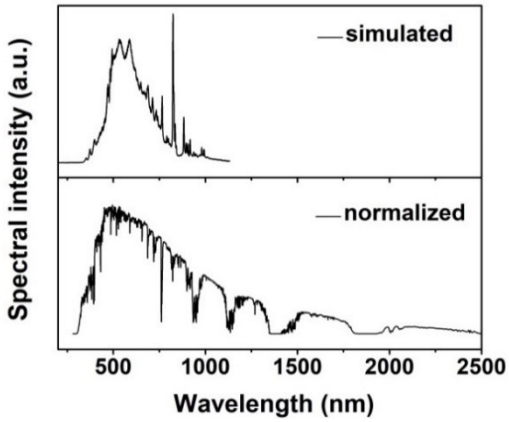

Figure S9. The irradiance intensity of the solar simulator (top) and the normalized spectral solar irradiance intensity of air mass 1.5 global (AM 1.5 G) tile solar spectrum (bottom). A solar simulator (Xenon Lamp) as a light source was used to generate simulated solar irradiation output through an AM 1.5 G filter, and the intensity of the solar beam was detected by optical fiber spectrometer. The energy of the simulated sunlight is concentrated in the range of 200-1100 nm. And in this case, the radiation spectrum of solar simulator matches with the normalized solar spectrum.

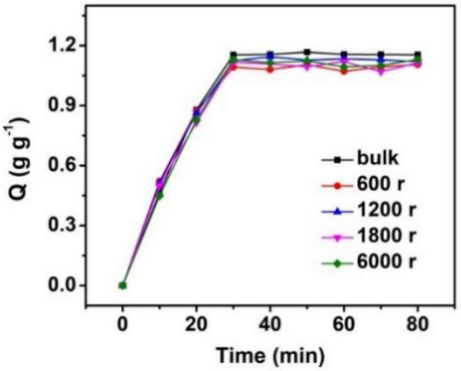

Figure S10. Water content (Q) in PVA-rCDs per gram of the corresponding xerogel (i.e. g g^{-1}) variation over time. Considering the water solubility as a crucial characteristic of PVA, the swelling behavior of the microgels was investigated by quantitatively measuring the water content. In detail, the as-prepared microspheres were dried at 60 °C overnight. Then a certain amount of the microgels (W_1) were immersed in deionized water for different time and collected by centrifugation. After removing the residual water by absorbent paper on the surface of the samples, the swelling samples were weighted (denoted as W_2).

$$Q = \frac{W_2 - W_1}{W_1}$$

The water transport rate (V) in hydrogels were calculated as:[9]

$$V=0.5Q_s/t$$

Where Q_s is the saturated water content, t is the half-swollen time. The Q_s values are 1.16, 1.07, 1.13, 1.12 and 1.09 g per gram of the corresponding xerogel (PVA-rCDs-bulk, -600 r, -1200 r, -1800 r, -6000 r, respectively), and the relevant V values are 0.0387, 0.0357, 0.0377, 0.0373 and 0.0363 g/min, respectively.

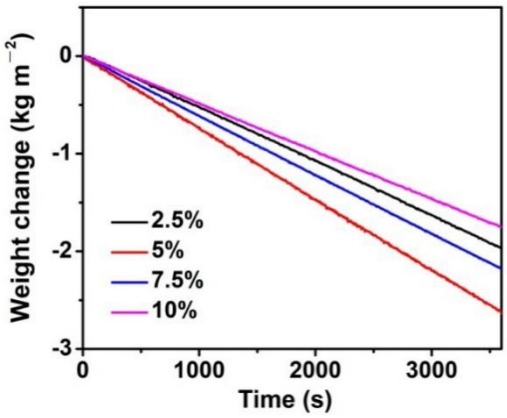

Figure S11. The mass change over time for microgels with different solid content under one sun. To study the influence of solid content, the solar steam generation performance of PVA-rCDs microgels with different solid content of 2.5%, 5%, 7.5% and 10% were evaluated for comparison. It is worth pointing out that the weight ratio of PVA to CDs is 1:0.15, so that the microgels with solid content of 5% is the PCM mentioned in the main text. The evaporation rates of PVA-rCDs microgels with solid content of 2.5%, 5%, 7.5% and 10% are 1.96, 2.62, 2.17 and 1.73 kg m^{-2} h^{-1}, respectively. Therefore, 5% solid content of the microgels is desirable.

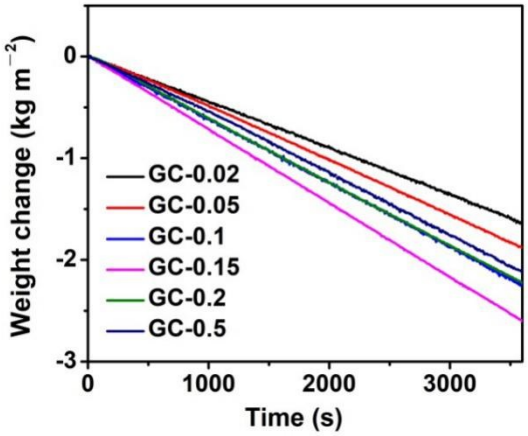

Figure S12. The mass change over time for GC-0.02，GC-0.05, GC-0.1, GC-0.15, GC-0.2 and GC-0.5. In order to obtain the optimal weight ratio of rCDs to PVA, we compare the water vapor generation properties of microgels with different relative amounts of rCDs. The microgels with rCDs/PVA ratio varied from 0.05:1, 0.1:1, 0.15:1, 0.2:1 to 0.5:1 were abbreviated as GC-0.02, GC-0.05, GC-0.1, GC-0.15, GC-0.2 and GC-0.5, respectively. Note that the solid content of all the rCP samples is 5%, GC-0.15 is the PCM mentioned in the main text. Impressively, GC-0.15 attains the maximum evaporation rate of 2.62 kg m^{-2} h^{-1}, higher than the values of 1.63, 1.88, 2.25, 2.23 and 2.11 kg m^{-2} h^{-1} for other samples form GC-0.02 to GC-0.5.

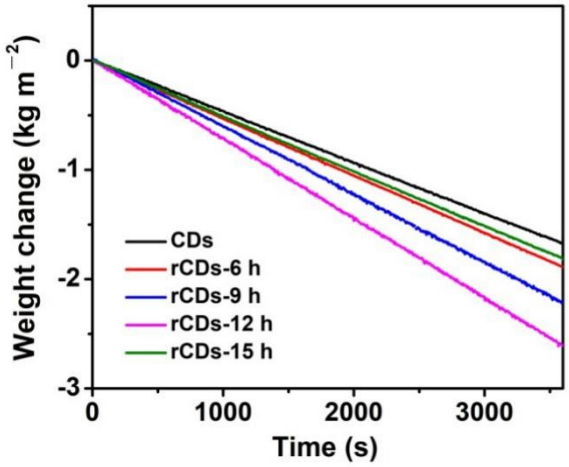

Figure S13 The weight changes over time for microgels with CDs of different oxidation degrees. The abbreviation of CDs to rCDs-15h is associated with the oxygen atoms contents of CDs for 24.81 at % , 31.72 at%, 23.97 at%, 22.24 at% and 21.37 at%.

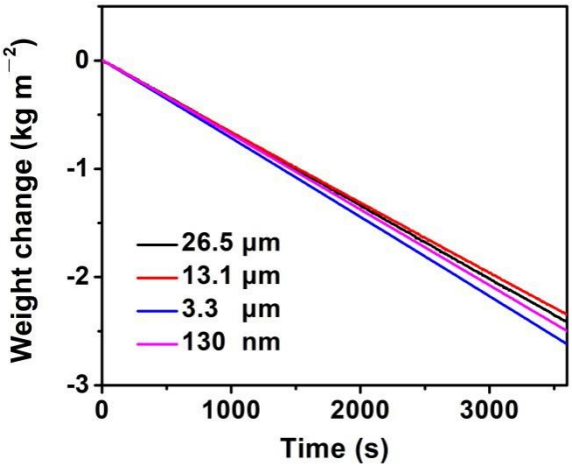

Figure S14 The weight changes over time for PVA-rCDs microgels with varying particle sizes, corresponding to the stirring rate from 600 r to 6000 r.

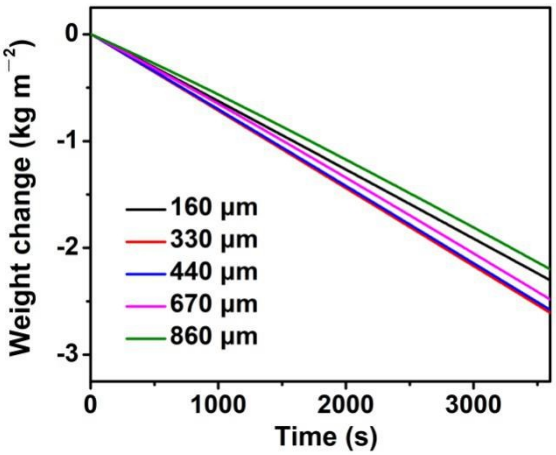

Figure S15. The mass change over time of PCM with different thickness. The PCM with thickness from 160 μm to 860 μm were prepared to evaluate their evaporation rates. All the thickness is measured by a thickness meter. Negligible variation for the evaporation rates were discerned in the thickness range of 330 μm to 670 μm, indicating appropriate thickness is in favor of the vapor generation. However, when the thickness beyond the range, the performance is slightly inferior, which might associate with the limited water transport or thermal localization.

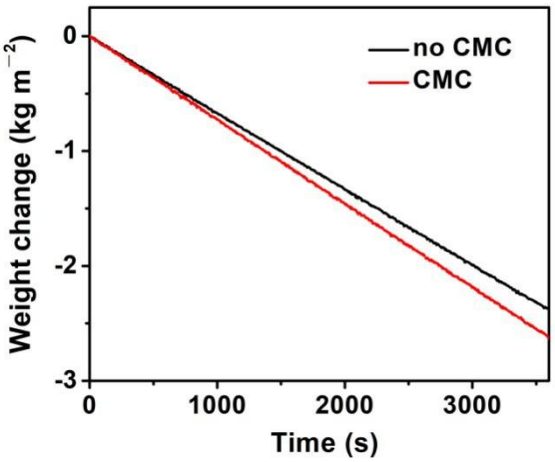

Figure S16. The mass change over time of PCM with and without CMC. The PCM-based evaporators with and without CMC as binder were prepared to estimate the solar-driven water evaporation. Weather adding CMC or not has a weak influence for the evaporation performance.

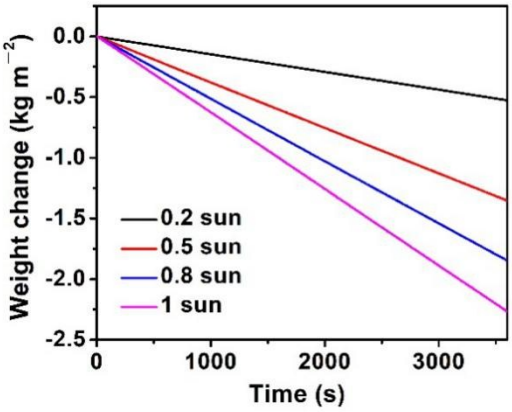

Figure S17. The mass change over time of PCM casted on filter paper. The evaporation rate of PCM casted on filter paper (200 um in thick) is approximately 2.26 kg m^{-2} h^{-1}, which, as expected, is in good agreement with the rate of extraction filtration with similar coating thickness (Figure S15). And the casting sample achieves the rates of 0.53, 1. 35 and 1.84 kg m^{-2} h^{-1} under 0.2 sun, 0.5 sun and 0.8 sun, respectively. As corroborated by the results, either the blade casting or the extraction filtration method was able to achieve impressive water evaporation performances, favorable for their commercial applications.

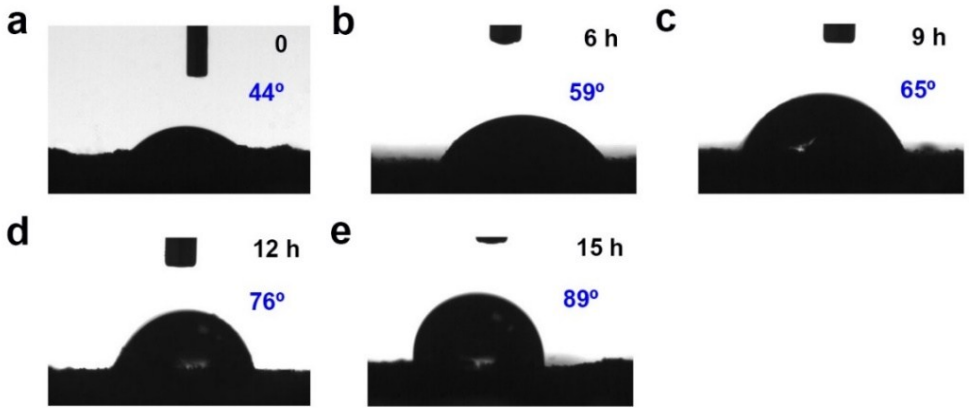

Figure S18. Water contact angle at 50th ms of the microgels using (a) CDs, (b) rCDs-6 h, (c) rCDs-9 h, (d) rCDs-12 h, (e) rCDs-15 h as additive. The wettability property is a key factor for solar driven evaporator, influencing the water transport to some extent. Therefore, the hydrophilicity of the contrastive samples using CDs with varying hydrazine reduction time (0 h, 6 h, 12 h, 15 h, respectively) were studied through the dynamic contact angles measurement. The contact angles of the samples are 44^{o} , 59^{o} , 65^{o} , 76^{o} and 89^{o} at 50th ms, and all the water drops permeate into the film eventually.

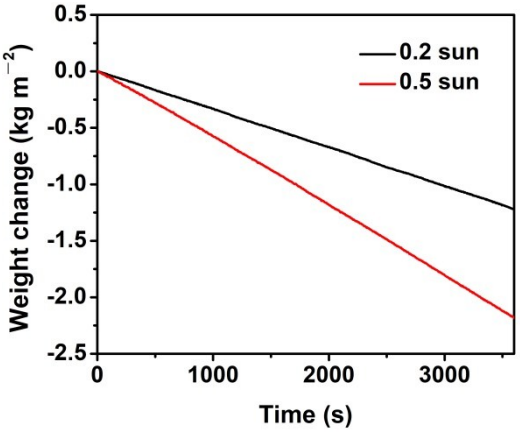

Figure S19. The mass change over time of 3D evaporators with θ=71° under 0.2 sun and 0.5 sun. The evaporation rate is 1.22 and 2.18 kg m^{-2} h^{-1}, respectively, both higher than the values of the novel evaporators list in table 1.

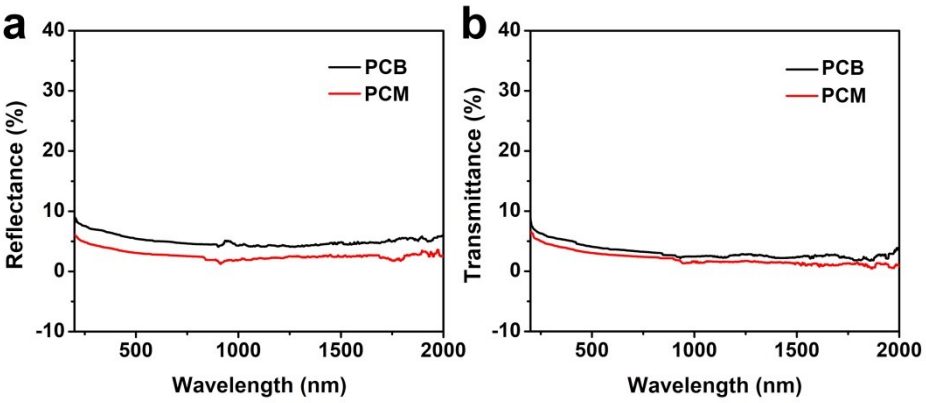

Figure S20. (a) Reflectance and (b) transmittance spectra of PCB and PCM in the wavelength range of 200–2000 nm. In light of the absorbance (A, A=1-*R*-*T*) of the test samples was gained based on reflectance (*R*) and transmittance (*T*) measurement,[10] the optical measurements was performed through a UV–vis–NIR spectrophotometer equipped with an integrated sphere. The PCM presents low reflectance (< 5%) and transmittance (< 5%) compared with the PCB in a broad wavelength range (200-2000 nm).

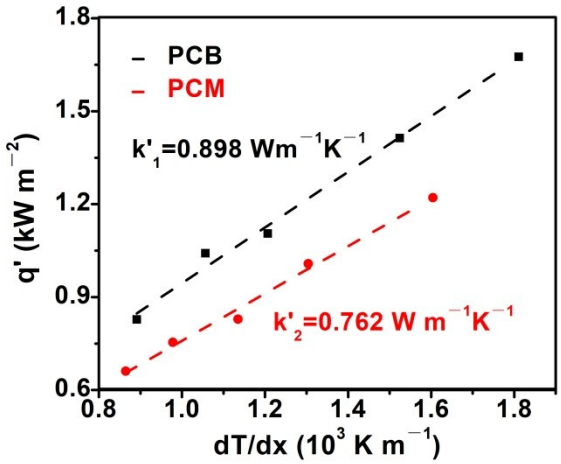

Figure S21. Thermal conductivity of wet PCB and PCM.

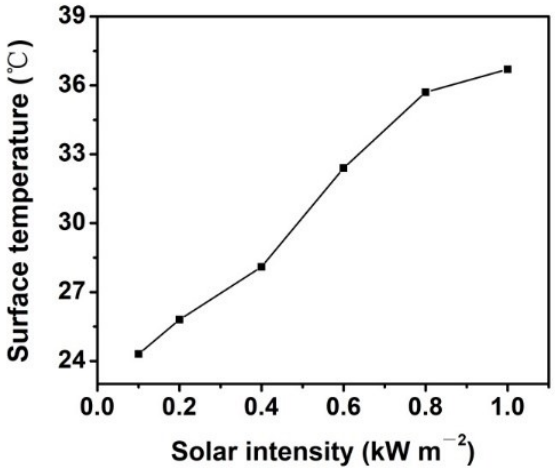

Figure S22. The surface temperature of PCM at different solar intensities.

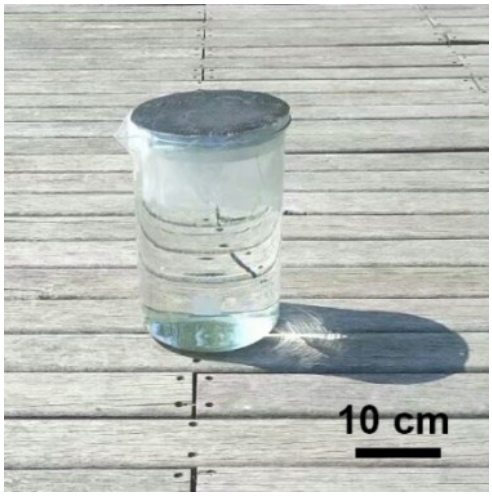

Figure S23. The solar vapor generation device for outdoor experiments.

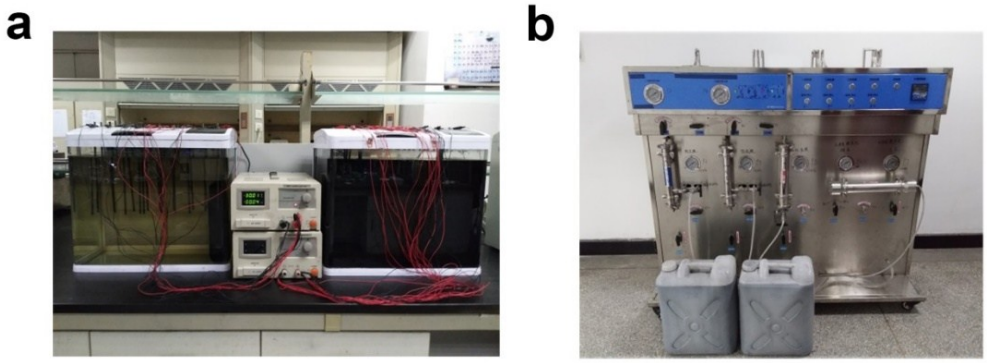

Figure S24. Photographs of (a) fabrication device of CDs, (b) a membrane separation experimental machine and the treated CDs. To evaluate the mass production and practical availability of CDs, the preparation and post-processing process are shown. Pairs of graphite rods as anodes and cathodes were immerged in deionized water in tanks, and constant voltage of 30 V was applied for two weeks to obtain black solution. Large graphite particles can be removed by a membrane separation experimental machine (BONA-GM-DMJ60, Jinan Bona Biological Technology Co., Ltd) equipped with nanofiltration membrane, and the collected CDs solution was subjected to concentration treatment via the machine. The process ensures the commercial feasibility of CDs.

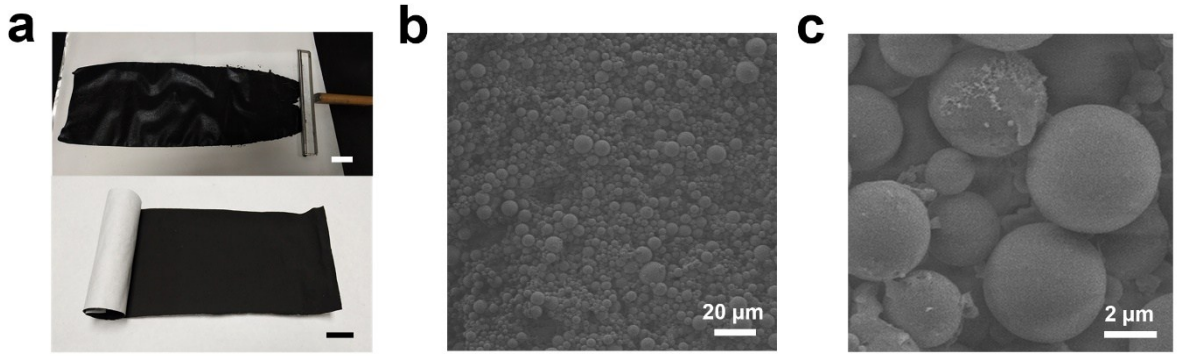

Figure S25. (a) Photograph of PCM blade casted on commercial filter paper by a rod coater (OPS, Japan), the scalebar is 5 cm. (b)-(c) SEM images of PCM coated on filter paper at different magnifications.

3. Supplementary Table

Table S1. The comparison of atomic contents of carbon and oxygen elements and the corresponding C/O atomic ratios of CDs.

	CDs	6 h	9 h	12 h	15 h
C content (at%)	66.33	67.93	70.25	69.76	73.53
O content (at%)	31.72	24.81	23.97	22.24	21.37
C/O ratio	2.091	2.738	2.931	3.136	3.440

Table S2. FO experiments at different draw solution concentrations with deionized water as the feed solution:

c_{Draw} (mol, NaCl)	π (kPa)	h (m)
0.05	247.88	25.27
0.1	495.76	50.54
0.15	743.64	75.80
0.2	991.53	101.07
0.25	1239.41	126.34
0.3	1487.3	151.61
0.4	1983.06	202.15
1	4957.64	505.36
2	9915.28	1011.73
5	24788.19	2526.82

Table S3. FO experiments at different draw solution concentrations with 3.5 wt% NaCl aqueous solution as the feed solution:

c_{Draw} (mol, NaCl)	π (kPa)	h (m)
1.5	4461.87	454.83
2	6940.69	707.51
2.5	9419.51	960.19
3	11898.33	1212.88
4	16855.97	1718.24
5	21813.61	2223.61

4. Supplementary calculation

4.1 Calculation S1: theoretical limit of evaporation rate

If the input solar energy is used for water evaporation, and other energy loss (i.e. heat radiation, heat convection, heat conduction) are not considered. The theoretical evaporation rate m is calculated as follows:[11]

$$m = \frac{\eta q_{solar}}{H_v}$$

η is the optical absorption coefficient (in an ideal condition, α=100%), q_{solar} is the power density of the sunlight at the surface of absorber (i.e., 1000 W m^{-2}=1000 J s^{-1} m^{-2}), H_v is the enthalpy change of liquid water to vapor.

We consider two cases:[12]

For 100 ℃ bulk water, H_v=2256.4 kJ kg^{-1},

$$m = \frac{100\% \times 1000 \times 3600}{2256.4 \times 1000} \approx 1.60 \text{ kg m}^{-2} \text{ h}^{-1}$$

For 25 ℃ bulk water, H_v=2441.7 kJ kg^{-1}

$$m = \frac{100\% \times 1000 \times 3600}{2441.7 \times 1000} \approx 1.47 \text{ kg m}^{-2} \text{ h}^{-1}$$

In this case, the theoretical limit of evaporation rate is 1.60 kg m^{-2} h^{-1} for 100 ℃ bulk water, and 1.47 kg m^{-2} h^{-1} for 25 ℃ bulk water.

4.2 Calculation S2: the temperature distribution

Thermal Model

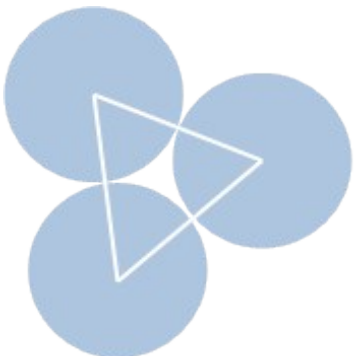

Figure S26. The geometric model showing the close-packed microgels and water channel. PVA-rCDs microgels (blue circle) are estabilished as dense packing model, and the interspace formed by the microspheres is the water channel.

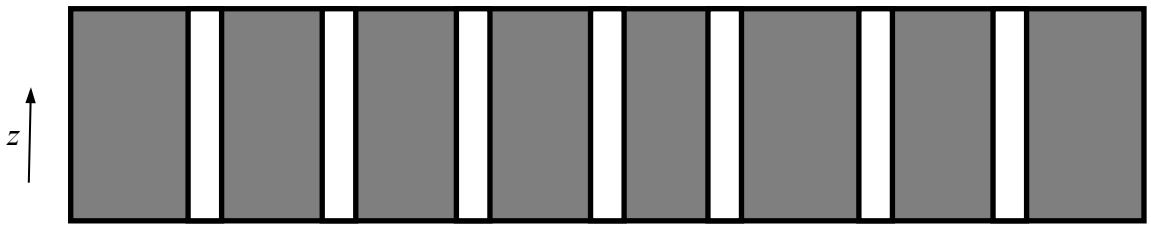

Figure S27. The macroscopic model of the evaporator representing the solid (microgels, grey

color) and water channel (white color).

Assuming *z* axis vertically upwards and taking the bottom of sample as the original point, the *z* value discussed below is the vertical distance from the origin.

The heat transfer equation

The heat transfer for water is given by the following equation:

$$\rho S_{1c}\frac{DH}{D\theta}=S_{1c}\frac{Dp}{D\theta}+kS_{1c}(\frac{\partial^2 T}{\partial x^2}+\frac{\partial^2 T}{\partial y^2}+\frac{\partial^2 T}{\partial z^2})+\Phi \tag{1}$$

That is:

$$\rho(\frac{\partial H}{\partial \theta}+u\frac{\partial H}{\partial x}+v\frac{\partial H}{\partial y}+w\frac{\partial H}{\partial z})=\frac{\partial p}{\partial \theta}+u\frac{\partial p}{\partial x}+v\frac{\partial p}{\partial y}+w\frac{\partial p}{\partial z}+k(\frac{\partial^2 T}{\partial x^2}+\frac{\partial^2 T}{\partial y^2}+\frac{\partial^2 T}{\partial z^2})+\Phi/S_{1c} \tag{2}$$

Considering the change in z direction, Equation (2) was simplified as:

$$\rho w\frac{\partial H}{\partial z}=k\frac{\partial^2 T}{\partial z^2}+w\frac{\partial p}{\partial z}+\Phi/S_{1c} \tag{3}$$

H is the enthalpy of liquid water, k and T are thermal conductivity and temperature of water, respectively, p is the pressure at position z. And u, v, w is flow velocity of water in x, y, z direction, respectively, θ is associated with time. Φ is the heat transferred from solid to water. S_{1c} is the cross-sectional area for the water channel.

For solid:

$$\rho_s S_{1s}\frac{\partial H}{\partial \theta}=k_s S_{1s}(\frac{\partial^2 T}{\partial x^2}+\frac{\partial^2 T}{\partial y^2}+\frac{\partial^2 T}{\partial z^2})-\Phi \tag{4}$$

For a steady state and one-dimensional equation:

$$S_{1s}k_s\frac{\partial^2 T_s}{\partial z^2}-\Phi=0 \tag{5}$$

T_s and k_s are the temperature and thermal conductivity of solid, S_{1s} is the cross-sectional area for solid (2.88×10^{-12} m^{-2}) around a single water channel.

And $d\Phi=\alpha(T_s-T)dA$ (6)

$$d\Phi=\alpha\pi d_e(T_s-T)dz \tag{7}$$

A is the contact area, and the heat transfer coefficient α caused by the natural convection between the solid and water can be calculated with Equation (8):

$$\alpha=\frac{\mathrm{Nu}\lambda}{\mathrm{L}} \tag{8}$$

Nusselt number Nu is calculated as follows:[13]

$$(Nu)_{D,f} = 0.87(Gr \bullet \Pr \bullet D/H)^{0.05}\ 10^{-4} < (Gr \bullet \Pr \bullet D/H)_{D,f} < 5\times10^{-2} \tag{9}$$

Where, Gr and Pr are Grashof and Prandtl numbers are calculated as:[14]

$$Gr = \frac{\rho^2 g \beta \Delta t L^3}{\mu^2} \tag{10}$$

$$\Pr = \frac{\mu C_p}{\lambda} \tag{11}$$

ρ is water density (995.6511 kg m^{-3}), g is gravitational acceleration, β is thermal expansion coefficient of water (0.000206 K^{-1}), Δt is the temperature difference between the average water temperature (assuming as 303K) and the bottom temperature, H and L is the length of water channel (0.0003 m), μ is viscosity of water (0.00079722 Pa s). λ is the thermal conductivity coefficient of water (0.6155 W m^{-1} K^{-1}), C_p is the specific heat capacity of water (4179.8 J kg^{-1} K^{-1}),[12] D is the hydraulic diameter d_e. Here, we obtained Nu=0.642 and α=1317 W m^{-2} K^{-1}.

The equilibrium equation

In steady-state condition, an equilibrium equation was given by the following expression:

$$\frac{S_c k_c S_{1s} k_s}{\alpha \pi d_e}\frac{\partial^3 T_s}{\partial z^3} - \frac{S_c w \rho_0 C_p S_{1s} k_s}{\alpha \pi d_e}\frac{\partial^2 T_s}{\partial z^2} - (S_s k_s + S_c k_c)\frac{\partial T_s}{\partial z} + S_c w \rho_0 C_p (T_s - T_0) = 0 \tag{12}$$

S_c is the total cross-sectional area for the water channels (0.0000815 m^{-2}), S_s is the projection area of the solid against the z direction (0.0002326 m^{-2}). The moist perimeter is calculated as 465 m. The hydraulic diameter d_e=4×S_c/moist perimeter=7.006×10^{-7} m^{-2}. The subscript "0" corresponding to the initial state at z=0 (e.g. ρ_0, T_0). w is flow velocity of water 2.796×10^{-6} m/s (calculated based on the evaporation rate).

The differential equation (12) was solved through deviation of corresponding univariate cubic equation:

$$\frac{S_c k_c S_{1s} k_s}{\alpha \pi d_e} x^3 - \frac{S_c w_0 \rho_0 C_{p,wet} S_{1s} k_s}{\alpha \pi d_e} x^2 - (S_s k_s + S_c k_c) x + S_c w_0 \rho_0 C_{p,wet} = 0 \tag{13}$$

With x_1, x_2, x_3 being the solutions of this equation,

Then:

$$T_s - T_0 = K_1 e^{x_1 z} + K_2 e^{x_2 z} + K_3 e^{x_3 z} \tag{14}$$

$$T_{wet} - T_0 = K_1\left(1 - \frac{S_{1s} k_s}{\alpha \pi d_e} x_1^2\right) e^{x_1 z} + K_2\left(1 - \frac{S_{1s} k_s}{\alpha \pi d_e} x_2^2\right) e^{x_2 z} + K_3\left(1 - \frac{S_{1s} k_s}{\alpha \pi d_e} x_3^2\right) e^{x_3 z} \tag{15}$$

And the boundary conditions (B.C.) were used to solve the K values:

B.C.:

①z=0, $T_{water}=T_0$=298 K; (16)

②z=300 μm, T_s=310 K, T_s is detected by an IR camera. (17)

③ $$\eta q_{solar} S + \alpha_{air-c} S_1 (T_{air} - T_{water}) = S_c w \rho_0 H_v + \alpha_{s-air} S_s (T_s - T_{air}) + \varepsilon \sigma S_s (T_{air}^4 - T_s^4) \quad (18)$$

Where η denotes the solar absorbance of the sample (90%), and q_{solar} is the power density of the sunlight at the surface of absorber (1000 W m^{-2}). S is the total projection area of the evaporator, $S=S_s+S_c=3.14\times10^{-4}$ m^{-2}. The evaporation area of curved surface for microgels S_1 is $\frac{\pi}{\sqrt{3}}$ time larger than that of the flat surface. $\alpha_{air\text{-}c}$ is the heat transfer coefficient for evaporation (2061 W m^{-2} K^{-1}, obtained from Equation (19)-(22)). T_{air} is ambient temperature (301 K), H_v is the enthalpy change of liquid water to vapor (2441.7 kJ kg^{-1}), $\alpha_{s\text{-}air}$ is the convection heat transfer coefficient (5 W m^{-2} K^{-1}). ε is the emissivity (0.97), σ is the Stefan−Boltzmann constant (5.67×10^{-8} W m^{-2} K^{-4}).[14] The Equation (18) depicts the most of the heat transfer processes (if not all), including the power flux consumed by evaporation, $S_c w \rho_0 H_v$, the convection loss to surrounding environment, $\alpha_{s\text{-}air}S_s(T_s-T_{air})$, the radiation loss to the ambient, $\varepsilon\sigma S_s$ ($T_s^4-T_{air}^4$), light energy input $\eta q_{solar} S$, the environmental compensation $\alpha_{air\text{-}c}S_s(T_s-T_{air})$.[15]

Additionally, the heat transfer coefficient for evaporation is given by:[16]

$$a_{air-c} = \frac{H_v V_v}{F(T_{air} - T)} \left(\frac{P_{sat}}{T} - \frac{P_a}{T_{air}}\right) \quad (19)$$

V_v is the velocity of the water vapour (m s^{-1}), calculated based on the identical conditions while shielding the sunlight. F=0.58 is a factor derived from calibrating the result using wet bulb thermometer equations. The saturated pressure in the atmosphere P_{sat}, the saturation pressure on the sample surface $P_{a,sat}$, and partial pressures of water vapor P_a are calculated as:

$$P_{sat} = 611.2 \exp\left[\frac{17.67(T - 273.16)}{T - 29.66}\right] \quad (20)$$

$$P_{a,sat} = 611.2 \exp\left[\frac{17.67(T - 273.16)}{T - 29.66}\right] \quad (21)$$

$$P_a = \frac{RH}{100} P_{a,sat} \quad (22)$$

Matlab software was used to solve the equations, and based on the B.C, the results we obtain were shown as follows.

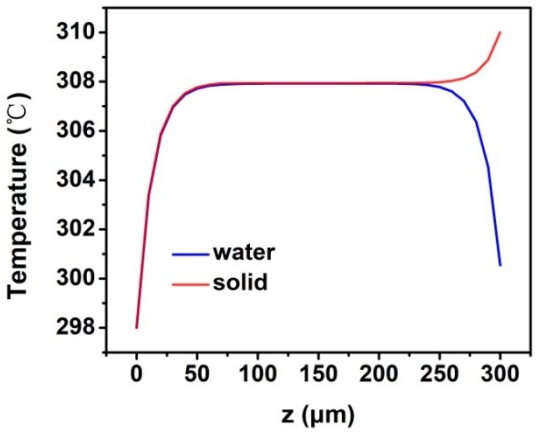

Figure S28. The temperature of solid and water relative to z axis.

4.3 Calculation S3: Q_{evap}/Q_{solar} ratio

According to the interface heat transfer equation (B.C. ③) mentioned above, the whole solar energy input (Q_{solar}) to the system is expressed as: $Q_{solar} = \eta q_{solar} S$. The consumed heat for evaporation (Q_{evap}) is: $Q_{evap} = S_c w \rho_0 H_v$. And the relative Q_{evap}/Q_{solar} ratio is caculated as follows:

Table S4. The Q_{evap}/Q_{solar} ratios of PCM at different solar intensities

	Q_{solar} (J)	Q_{evap} (J)	Q_{evap}/Q_{solar} ratio
0.2 sun	0.05652	0.14695	2.60
0.5 sun	0.1413	0.33649	2.38
1 sun	0.2826	0.55372	1.96
2 sun	0.5652	0.72623	1.28
3 sun	0.8478	1.08614	1.28
4 sun	1.1304	1.43968	1.27

5. Supplementary References

1. J. Yao and G. Yang, *J. Mater. Chem. A*, 2018, **6**, 3869-3876.
2. Q. Jiang, L. Tian, K.-K. Liu, S. Tadepalli, R. Raliya, P. Biswas, R. R. Naik and S. Singamaneni, *Adv. Mater.*, 2016, **28**, 9400-9407.
3. H. Li, Y. He, Y. Hu and X. Wang, *ACS Appl. Mater. Interfaces* **2018**, 10, 9362.
4. S. Suku, T. Knipfer and W. Fricke, *Ann. Bot.*, 2014, **113**, 385-402.
5. M. J. Chrispeels, C. Maurel, *Plant Physiol*, 1994, **105**, 9-13.
6. E. Steudle, R. Oren and E. D. Schulze, *Plant Physiol*, 1987, **84**, 1220-1232.
7. I. Pawlowicz and K. Masajada, *Gene*, 2019, **687**, 166-172.
8. L.Taiz and E. Zeiger, Plant physiology, 3 rd edn, *Ann. Bot.* **2003**.
9. X. Zhou, F. Zhao, Y. Guo, Y. Zhang and G. Yu, *Energ. Environ. Sci.* 2018, **11**, 1985-1992.
10. T. Li, H. Liu, X. P. Zhao, G. Chen, J. Q. Dai, G. Pastel, C. Jia, C. J. Chen, E. Hitz, D. Siddhartha, R. G. Yang and L. B. Hu, *Adv. Funct. Mater.*, 2018, **28**, 1707134.
11. Y. Yang, R. Zhao, T. Zhang, K. Zhao, P. Xiao, Y. Ma, P. M. Ajayan, G. Shi and Y. Chen, *ACS Nano*, 2018, **12**, 829-835.
12. D. R. Lide, CRC press, Boca Raton, FL, USA, **2009**.

13. V. T. Morgan, *Advances in Heat Transfer*, 1975, **11**, 199-264.
14. S. Kumar, S. K. Prasad and J. Banerjee, *Appl. Math. Model.* 2010, **34**, 573-592.
15. H. M. Song, Y. H. Liu, Z. J. Liu, M. H. Singer, C. Y. Li, A. R. Cheney, D. X. Ji, L. Zhou, N. Zhang, X. Zeng, Z. M. Bei, Z. F. Yu, S. H. Jiang and Q. Q. Gan, *Adv. Sci.*, **2018**, 5, 1800222.
16. I. S. Cole and D. A. Paterson, Corros. *Eng. Sci. Technol.*, 2006, **41**, 67-76.